surfaces

MDPI

Article

Fabrication and Characterization of High-Performance Channel Electron Multipliers Using Alternating Acid and Base Etching and Atomic Layer Deposition

Zexun Hu [1,2,3], Xiaoqing Cong [2,3,*], Yunsheng Qian [4,*], Shulin Liu [5], Jiaqi Zhu [2,3], Heng Zhao [2,3], Jian Wang [2,3], Yan Cheng [2,3], Pengjie Niu [2,3] and Longhui Li [1,2,3]

1 Kunming Institute of Physics, China North Industries Group Corporation, Kunming 650223, China; zexunhu@163.com (Z.H.)
2 North Night Vision Technology (Nanjing) Research Institute Co., Ltd., China North Industries Group Corporation, Nanjing 211100, China
3 North Night Vision Technology Co., Ltd. Nanjing Branch, China North Industries Group Corporation, Nanjing 211100, China
4 College of Electronic Engineering and Optoelectronic Technology, Nanjing University of Science and Technology, Nanjing 210094, China
5 Institute of High Energy Physics, Chinese Academy of Sciences, Beijing 100049, China
* Correspondence: cong_stone@163.com (X.C.); yshqian@njust.edu.cn (Y.Q.)

Abstract

Channel electron multipliers (CEMs) are continuous dynode vacuum electronic devices used in residual gas analysis and mass spectrometry. Owing to the unique structure and intricate fabrication process of CEMs, developing ultra-high-gain, low-noise devices has long been a major engineering challenge worldwide. The CEM was fabricated from lead silicate glass by preform preparation, capillary drawing, inlet flaring, outlet bending, inlet shaping, cleaning, hydrogen reduction, sandblasting isolation, etching, electron-beam evaporation and atomic layer deposition. We characterized the inner-wall morphology and electrical properties following alternating acid and base etching and atomic layer deposition (ALD) using SEM/EDS, AFM, XPS and electrical measurements. Rounded elemental-lead particles (237 ± 31 nm in diameter) were observed on the channel wall after high-temperature hydrogen reduction. Alternating etching with 1.2 mol/L HCl and 8 wt.% NaOH reduced the root-mean-square roughness (Rq) from 1.28 to 0.15 nm. This reduction is hypothesized to result from the dissolution of elemental Pb by HCl and SiO_2 by NaOH. At 2.0 kV, pulse gain increased from 2.00×10^6 to 8.25×10^6, while dark count rate decreased from 54.23 to below 2 counts/s. A nominally 5.5 nm Al_2O_3 coating deposited by ALD further increased gain fourfold to 3.30×10^7. After an accumulated output charge of 0.158 C, analog gain loss decreased from 89% to 11%. Based on CST Studio Suite 2021, a three-dimensional electromagnetic simulation model of CEM was built. The simulation results show that the pulse full width at half maximum (FWHM) of CEM is 6.4 ns, which is basically consistent with the measured result of 8 ns. Increasing protrusion thickness from 0 to 0.4 mm reduced simulated gain from 8.71×10^6 to 2.60×10^6 at 2.0 kV. The combined experimental and simulation results provide a basis for developing CEMs with improved gain, noise performance and lifetime.

Keywords: channel electron multiplier; electron multiplication; alternating acid and base etching; atomic layer deposition; CST simulation

Academic Editor: Aleksey Yerokhin

Received: 19 October 2026
Revised: 11 November 2026
Accepted: 16 November 2026
Published: 19 November 2026

Copyright: © 2026 by the authors. Licensee MDPI, Basel, Switzerland. This article is an open access article distributed under the terms and conditions of the Creative Commons Attribution (CC BY) license.

1. Introduction

Channel electron multipliers (CEMs) are vacuum detectors that amplify weak particle signals through secondary electron emission from a continuous dynode surface. It offers high gain, low noise and low power consumption [1]. CEMs are widely used in residual gas analyzers, mass spectrometers, X-ray photoelectron spectrometers and ultraviolet spectrometers to detect ions, electrons and ultraviolet photons [2–6]. As key detectors in analytical instruments, CEMs require sufficient and stable gain to ensure that their output exceeds the noise level and discrimination threshold of the readout electronics, thereby reducing the probability of missing weak signals. A low dark count rate reduces detector background and improves the signal-to-noise ratio under low-flux conditions. Consequently, instrument manufacturers have a strong demand for high-performance CEMs.

Previous studies have investigated CEM performance in terms of multiplication theory, electron collection and noise. Adams and Manley [1] developed a gain model covering the straight and curved sections. Chen et al. [7] increased collection efficiency to 99.8% using a new focusing system, while Manalio et al. [8] improved detection efficiency by more than a factor of three by coating the inlet cone with MgO. Grzeszczak et al. [9–11] found that dark-current fluctuations exhibited typical flicker-noise behavior at low CEM operating currents and transitioned to white noise at sufficiently high output currents.

Microchannel plates (MCPs) contain millions of straight channels, and the effects of fabrication processes such as etching and deposition on their performance have been studied in detail [12,13]. A CEM, however, consists of a single curved channel and differs from an MCP in both fabrication sequence and structural parameters. Few studies have examined the complex relationships among CEM fabrication, morphology, and electrical performance. Table 1 compares the present CEM study with the MCP study by Li et al. [12]. The CEM studied here differs from an MCP in its structural parameters: it has a three-section geometry comprising a flared inlet, a straight section and a curved section, and its channel diameter is on the millimeter scale. Both alternating acid and base etching and atomic layer deposition (ALD) were incorporated into CEM fabrication. The channel wall morphology, composition and roughness were characterized, and pulse gain, dark count rate and lifetime were systematically measured. An electron-transport model was established to analyze the effects of local protrusion geometry on electron transport and multiplication, providing a basis for process optimization.

Table 1. Comparison of the present CEM study with the MCP study by Li et al. [12].

Comparison Item	Present CEM Study	Li et al. [12], MCP Study
Structure	Flared inlet, straight and curved sections	Straight channels
Channel diameter	Millimeter scale	Micrometer scale
Alternating acid and base etching	Yes	Yes
Atomic layer deposition	Yes	No
Wall morphology and composition	Yes	Yes
Wall roughness	Yes	Yes
Pulse gain	Yes	No
Dark count rate	Yes	No
Lifetime	Yes	No
Simulation	Yes	No

2. Materials and Methods

2.1. Multiplication Principle

The multiplication principle is illustrated in Figure 1a. An incident particle strikes the channel wall and releases secondary electrons. The electric field accelerates these

electrons toward the wall, where repeated impacts generate an electron avalanche that exits the channel. Figure 1b defines the inlet cone angle A, cone width W, cone height H, straight-section length L, curved-section radius R, channel inner diameter d and capillary outer diameter D.

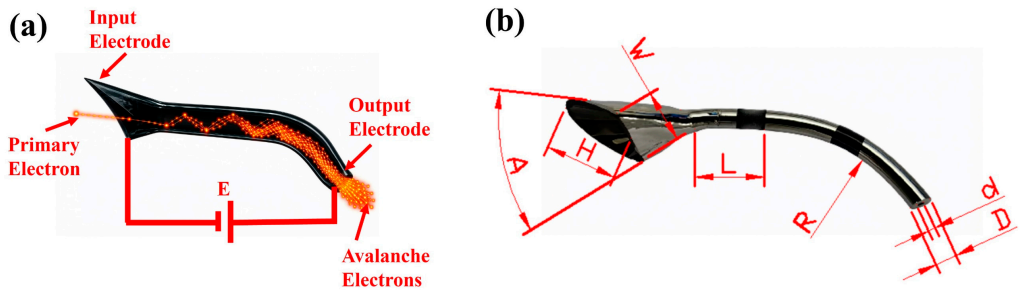


Figure 1. CEM overview: (**a**) operating principle; (**b**) geometric parameters.

2.2. Fabrication Process

The CEM substrate was lead silicate glass with the composition given in Table 2.

Table 2. Composition of the lead silicate glass.

Component	PbO	SiO_2	Bi_2O_3	BaO	Al_2O_3
Mole fraction (%)	23.6	64.2	3.6	4.9	3.6

The fabrication sequence is shown in Figure 2 and comprises the following steps.

(1) Preform preparation: A cylindrical preform with a 10 mm inner diameter and a 30 mm outer diameter was produced by turning and drilling.
(2) Capillary drawing: The preform was drawn at 700 °C to a capillary with a 1 mm inner diameter and a 3 mm outer diameter.
(3) Inlet flaring: A conical graphite mold was heated to 800 °C, and the capillary inlet was brought into contact with the mold to form a cone.
(4) Outlet bending: The rear section was bent into an arc at 750 °C.
(5) Inlet shaping: The base of the inlet cone was ground flat with 120-grit silicon carbide abrasive to form the final flared geometry.
(6) Cleaning: The CEM was ultrasonically cleaned in anhydrous ethanol (99.7% purity).
(7) Hydrogen reduction: The CEM was reduced in a hydrogen atmosphere at 480 °C. During hydrogen reduction, PbO in the material was reduced to elemental Pb, as shown in Equation (1), giving the CEM electrical conductivity:

$$PbO + H_2 = Pb + H_2O \quad (1)$$

(8) Sandblasting isolation: The resistive layer near the inlet was isolated by sandblasting with 120-grit silicon carbide abrasive.
(9) Etching: This study introduces alternating acid and base etching to control channel wall morphology. Based on the MCP etching process reported by Li et al. [12], the solution concentrations and stirring rate were increased to account for the three-section CEM geometry. The acid was dilute HCl at approximately 1.2 mol/L, and the base was NaOH at a mass fraction of approximately 8%. Each solution was stirred magnetically at 1500 rpm. Following each acid or base treatment, the CEM was ultrasonically cleaned in pure water at 40 kHz and 300 W. The complete sequence is given in Table 3.

Table 3. Alternating acid and base etching sequence.

Step	Treatment	Duration or Instruction
1	Acid treatment with stirring	45 min
2	Ultrasonic cleaning in pure water	5 min
3	Base treatment with stirring	45 min
4	Ultrasonic cleaning in pure water	5 min
5	Repeat steps 1–4	Two additional cycles

(10) Electron-beam evaporation: A nickel–chromium alloy was deposited uniformly at the designated front, middle and rear electrode positions.

(11) Atomic layer deposition: This study introduces ALD to form an Al2O3 layer on the CEM channel wall. Deposition was performed using a BENEQ TFS500 system with high-purity N2 (99.99%) as the carrier gas and trimethylaluminum (TMA) and H2O as the precursors. The surface reactions are given in Equations (2) and (3). The TMA/N2/H2O/N2 pulse and purge sequence was 0.8/30/0.6/30 s per cycle. After deposition of the Al2O3 layer, the samples were held at 300 °C for 5 h and then cooled with the equipment. To examine film-thickness uniformity at different CEM locations, 400 deposition cycles were performed to produce a film thick enough for scanning electron microscopy measurements. Al2O3 film thickness affects gain [14]; in the CEM fabrication process, 55 cycles were deposited with reference to the MCP deposition process [14]:

$$AlOH^{*} + Al(CH_3)_3 \rightarrow AlOAl(CH_3)_2^{*} + CH_4 \uparrow \quad (2)$$

$$Al(CH_3)_2^{*} + H_2O \rightarrow Al(OH)^{*} + CH_4 \uparrow \quad (3)$$

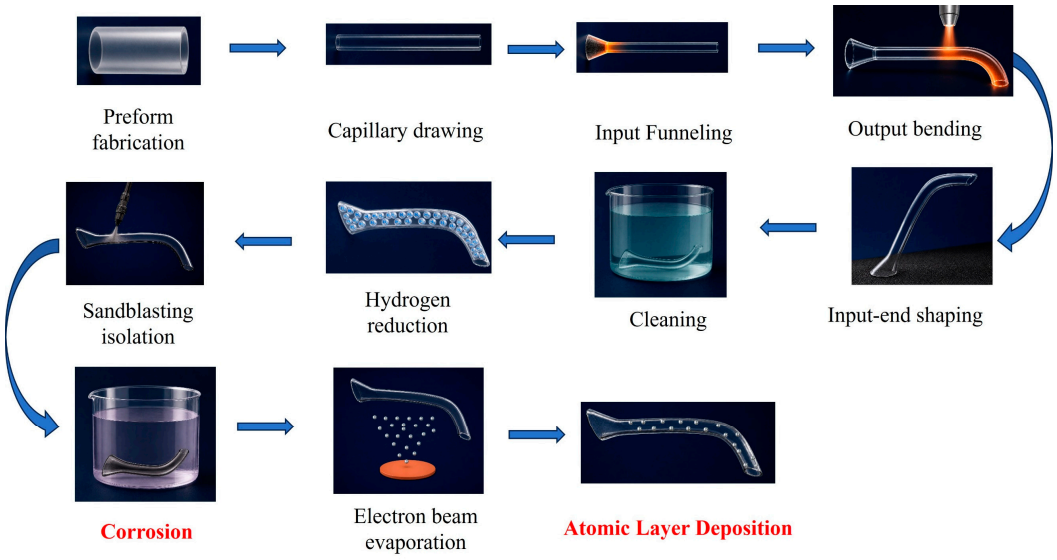


Figure 2. CEM fabrication sequence.

The CEM fabricated by this procedure is shown in Figure 1b, and its geometric parameters are listed in Table 4. Its compact dimensions make it suitable for use in a range of analytical instruments.

Table 4. CEM geometric parameters.

Parameter	A (°)	W (mm)	H (mm)	L (mm)	R (mm)	d (mm)	D (mm)
Value	38	7.2	9.9	9.5	25	1	3

2.3. Experimental Design

Three process conditions were used to separate the effects of etching and ALD (Table 5). Case 1 received neither treatment; Case 2 received etching only; and Case 3 received ALD based on the same etching. Comparing Cases 1 and 2 isolates the effect of etching, while comparing Cases 2 and 3 estimates the additional effect of ALD.

Table 5. CEM processing conditions.

Condition	Etching	Atomic Layer Deposition
Case 1	No	No
Case 2	Yes	No
Case 3	Yes	Yes

3. Results and Discussion

3.1. Al_2O_3 Film-Thickness Uniformity

Film thickness at different CEM locations was measured by scanning electron microscopy (SEM). The CEM was destroyed for the measurements, and the results are shown in Figure 3. After 400 deposition cycles, film thicknesses at the flared inlet, straight section and curved section were 42.5, 41.1 and 39.7 nm, respectively. The ratio of the maximum to minimum thickness was 1.07, the mean thickness was 41.1 nm, and the mean growth per cycle was 0.10 nm. For the fabricated CEMs, 55 cycles were deposited, giving a nominal thickness of 5.5 nm.

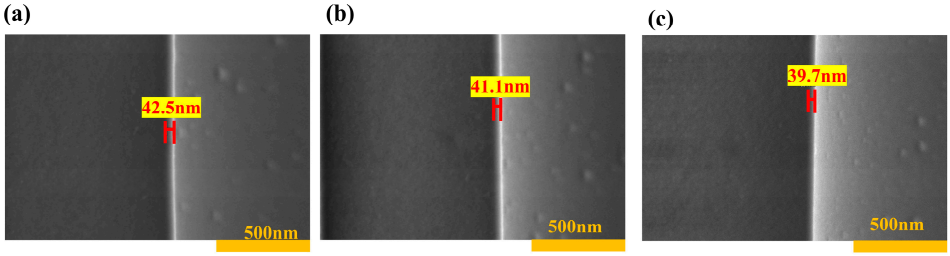


Figure 3. Film thickness at different CEM locations after 400 deposition cycles: (**a**) flared inlet; (**b**) straight section; (**c**) curved section.

3.2. Aluminum on the Channel Wall

The Al distribution on the channel wall was analyzed using an X-ray photoelectron spectrometer (XPS) in narrow-scan mode (Figure 4). The measurement was performed at the flared inlet and required destructive testing. No distinct peak was observed for Case 2 over the binding-energy range of 70–80 eV; the signal was comparable to the background, indicating only trace Al on the wall. In contrast, Case 3 exhibited a distinct Al 2p peak at approximately 74.2 eV. The substantial increase in Al 2p intensity after deposition supports the presence of an aluminum-containing oxide layer at the analyzed location and is consistent with the expected Al_2O_3 film. Together with the film-thickness measurements after 400 cycles in Figure 3, these results suggest that a uniform Al_2O_3 film formed on the CEM channel wall.

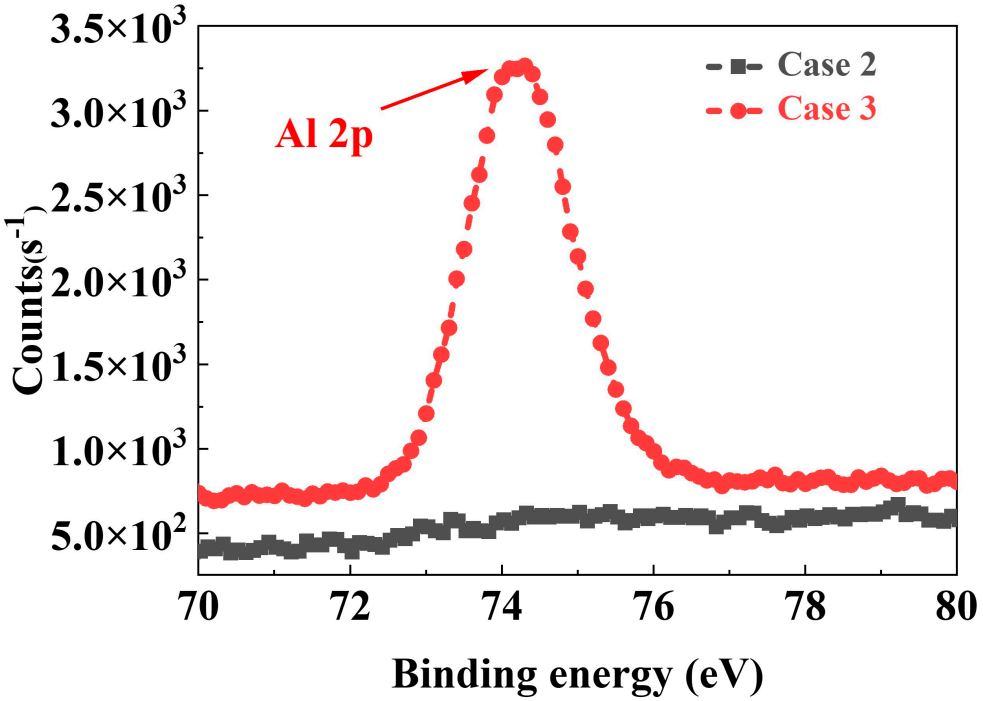


Figure 4. Al 2p XPS spectra of the channel wall.

3.3. Channel Wall Morphology

Surface particles on the fabricated CEMs were examined by SEM. The measurement was performed at the flared inlet and required destructive testing. The spatial distribution of Pb was mapped by energy-dispersive X-ray spectroscopy (EDS) at an accelerating voltage of 20 kV. The morphology and Pb maps are shown in Figure 5. Rounded particles of different sizes were distributed across the Case 1 surface. The larger particles highlighted by red circles in Figure 5a had a diameter of 237 ± 31 nm. The Pb distribution coincided with the particle distribution, indicating that Pb was their principal constituent. We attribute these particles to elemental lead produced during high-temperature hydrogen reduction, which volatilized at high temperature and condensed on the channel wall during cooling. Aggregation during condensation produced the rounded particles. Alternating acid and base etching removed these particles in Cases 2 and 3, leaving smooth, particle-free surfaces and a more uniform Pb distribution, as shown in Figure 5b,c,e,f.

3.4. Channel Wall Roughness

Channel wall roughness was measured by atomic force microscopy (AFM) in tapping mode (Figure 6). The measurement was performed at the flared inlet and required destructive testing. Comparing Figures 6a and 6b shows that alternating acid and base etching reduced the peak-to-valley height from 8.6 to 1.1 nm and the root-mean-square roughness (Rq) from 1.28 to 0.15 nm. Large protrusions were evident in Case 1 but absent in Case 2, indicating that etching removed protrusions and reduced surface roughness. Comparing Figures 6b and 6c shows that, after ALD, the peak-to-valley height decreased further to 0.39 nm and Rq to 0.05 nm, indicating further improvement in the measured surface morphology.

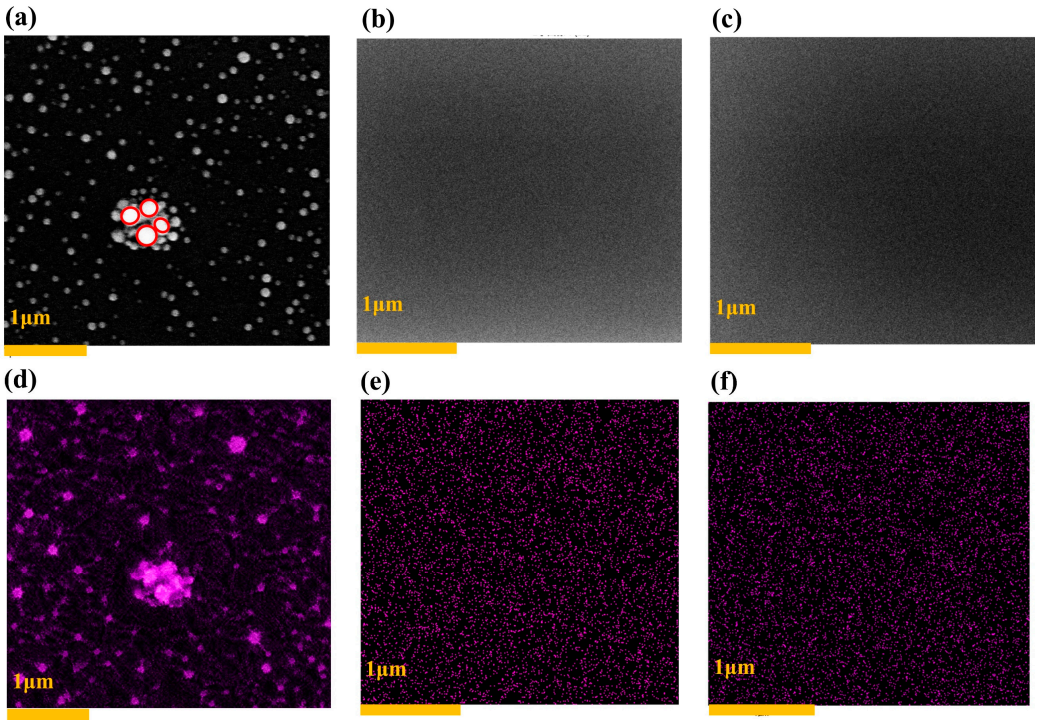


Figure 5. Channel wall morphology and Pb elemental maps: (**a**–**c**) SEM images of Cases 1–3; (**d**–**f**) corresponding Pb maps.

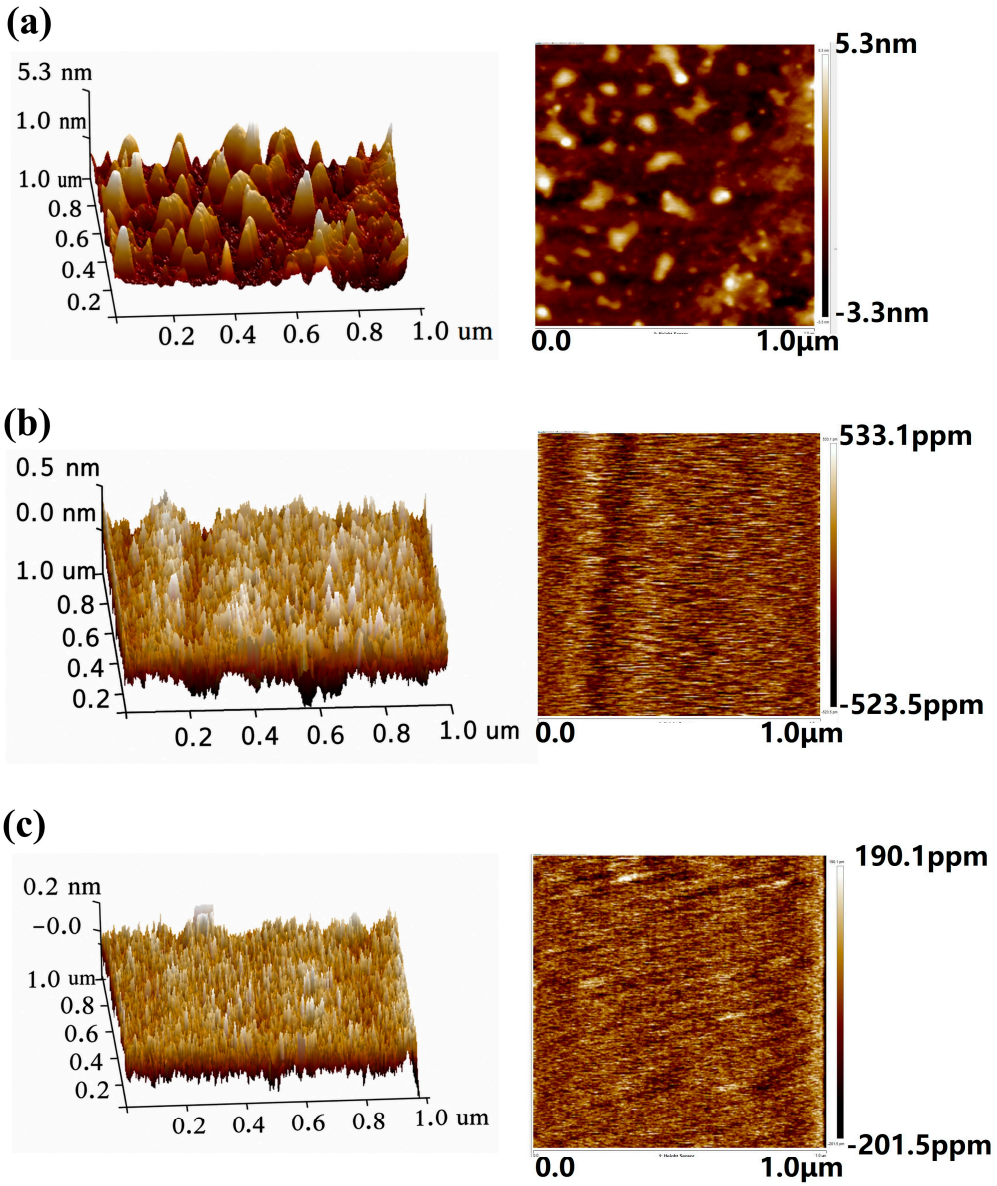


Figure 6. AFM measurements of channel wall roughness: (**a**) Case 1; (**b**) Case 2; (**c**) Case 3.

3.5. Electrical Characterization

The CEM electrical test arrangement is shown in Figure 7a and supports both counting and direct-current analog modes. Both measurements were performed at a pressure of 1×10^{-4} Pa. In counting mode, a signal generator provided two voltage outputs: one drove a UV LED, and the other synchronously triggered an oscilloscope. Ultraviolet light from the LED illuminated a gold photocathode to generate electrons. Adjusting the LED drive voltage changed its brightness so that the photocathode operated in the single-electron regime. After multiplication in the CEM, the electrons were collected by the anode, and the resulting signal was sent to the oscilloscope. Pulse gain, dark count rate and pulse full width at half maximum (FWHM) were determined from the recorded voltage signals. In analog mode, an electronic ballast drove a low-pressure mercury lamp. A filter between the lamp and gold photocathode adjusted the incident ultraviolet intensity and hence the CEM input current I_{in}. The multiplied output was collected by the anode, and the output current I_{out} was measured with an electrometer. Analog gain was calculated as I_{out}/I_{in}. This mode was also used for lifetime testing. In addition, with no input, a voltage of 2.2 kV was

applied to the CEM and the circuit current was measured. The CEM bulk resistance was calculated as the ratio of the applied voltage to the circuit current.

The electrode biasing arrangement is shown in Figure 7b. The potentials of the gold photocathode, CEM inlet, CEM outlet and anode are denoted by U_{ca}, U_{in}, U_{out} and U_{an}, respectively. The applied potentials are specified in Equations (4)–(7). The inlet-to-photocathode potential difference was 300 V, and the outlet-to-inlet potential difference Ucem was varied as the operating voltage. The anode bias followed Equation (7).

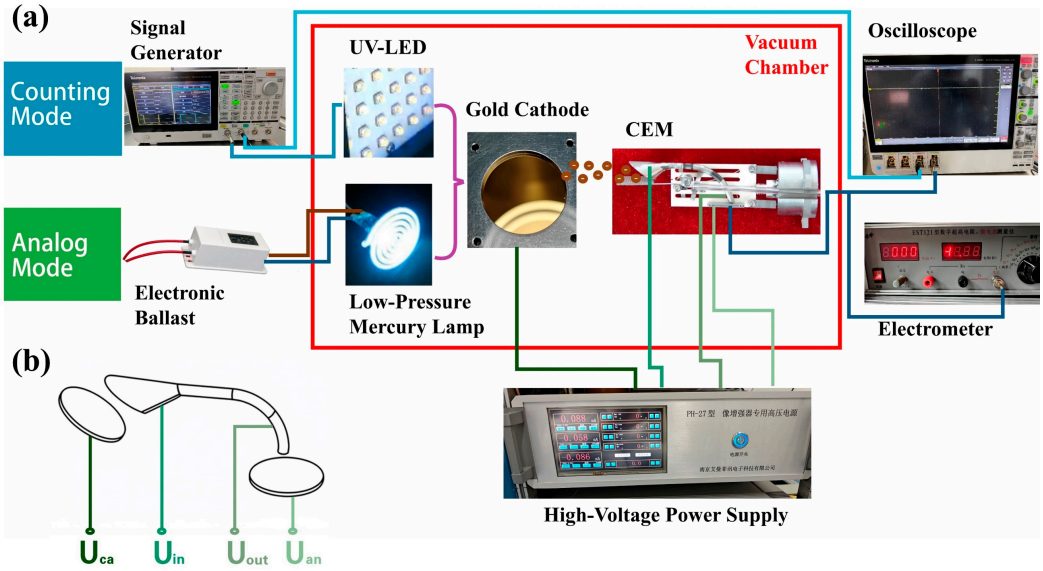


Figure 7. CEM electrical characterization: (**a**) test arrangement; (**b**) applied electrode potentials.

$$U_{ca} = -300V \quad (4)$$

$$U_{in} = 0V \quad (5)$$

$$U_{out} = U_{in} + U_{cem} \quad (6)$$

$$U_{an} = U_{out} + 100 \quad (7)$$

Here, U_{ca} is the gold photocathode potential, U_{in} is the CEM inlet potential, U_{out} is the CEM outlet potential, U_{cem} is the positive outlet-to-inlet potential difference (hereafter the operating voltage), and U_{an} is the anode potential.

Using this test arrangement and evaluation method, the same sample was measured 10 times. The measurement precision was 10.2% for DC gain, 14.7% for pulse gain, 8.9% for dark count rate and 1% for bulk resistance.

Pulse gain increased with operating voltage in all three cases (Figure 8). The increase became less pronounced above 2.2 kV, possibly because the CEMs were approaching saturation. Case 1 consistently exhibited lower gain than Case 2. At 2.0 kV, Case 2 had a gain of 8.25×10^6, approximately 4.1 times the Case 1 value of 2.00×10^6. The protrusions visible in Figure 6a may have impeded further secondary-electron multiplication and thereby reduced the Case 1 gain. Case 3 consistently exceeded Case 2: at 2.0 kV, its gain was 3.30×10^7, four times the Case 2 value. We attribute this enhancement to the higher secondary-electron yield of Al_2O_3 (3.95) relative to lead silicate glass (2.75). Overall, gain increased substantially after alternating acid and base etching and deposition, reaching 16.5 times the untreated value.

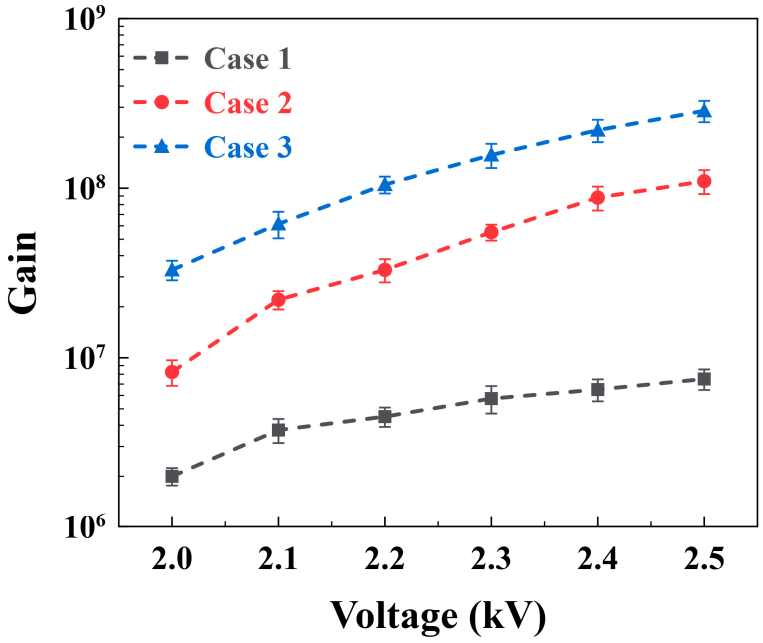


Figure 8. Pulse gain as a function of operating voltage.

Figure 9 shows dark count rate as a function of operating voltage in pulse mode. Case 1 exhibited a dark count rate of at least 54.23 counts/s at every tested voltage. We attribute this high background to discharge from the rounded Pb particles in Figure 5a under high voltage. The dark count rates of Cases 2 and 3 increased with voltage but remained below 2 counts/s. The dark count rates of Cases 3 and 2 were similar: at 2.0 kV, they were 0.48 and 0.42 counts/s, respectively, indicating no significant effect of ALD on the dark count rate. To further evaluate the fabrication process and measurement method, a small-batch validation was performed using the same process and method (20 devices). After alternating acid and base etching and deposition, gain at 2 kV reached 15.2 times the untreated value and the dark count rate fell to 0.92% of the untreated value. These results were broadly consistent with those for a single CEM, for which gain reached 16.5 times and the dark count rate fell to 0.89% of the untreated value.

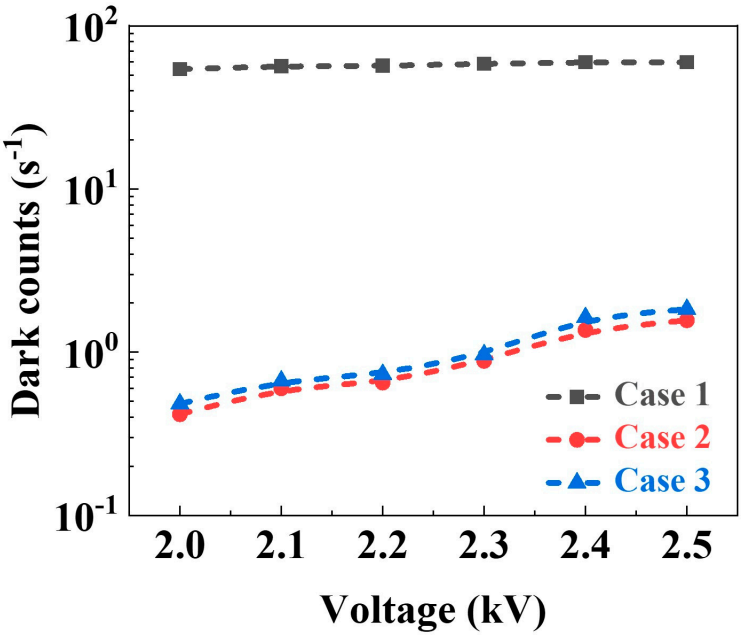


Figure 9. Dark count rate as a function of operating voltage in pulse mode.

https://doi.org/10.3390/surfaces9040097

The bulk resistances of Cases 1, 2 and 3 were 69, 81 and 82 MΩ, respectively. We hypothesize that the increased bulk resistance observed in Cases 2 and 3 resulted from the removal of the spherical lead particles shown in Figure 5, which reduced the electrical conductivity of the CEM.

The lifetime test results in simulation mode are shown in Figure 10. According to the requirements of the residual gas analyzer manufacturer and considering the influence of factors such as vacuum level, detection gas, and operating voltage, the CEM output current during long-term operation is equivalent to 1 nA. Based on 24 h daily operations over 5 consecutive years, the cumulative output charge is calculated to be 0.158 C. Cases 2 and 3 were subjected to accelerated lifetime testing in analog mode. The input current was adjusted to maintain an output current of 4.38 μA for 10 h, delivering the same accumulated charge as five years of operation in the stated application. Comparing gain before and after the test showed a pronounced decrease for Case 2: at 1.0 kV, gain fell from 1.20×10^4 to 1.32×10^3, a loss of 89%. Case 3 showed only a modest decrease from 8.00×10^4 to 7.12×10^4 at 1.0 kV, a loss of 11%. Under the same accumulated output charge, the fractional gain loss of Case 3 was approximately 0.12 times that of Case 2, demonstrating improved CEM lifetime after ALD.

3.6. Simulation Analysis

Simulations were performed in the Particle Tracking Studio of CST Studio Suite 2021. A three-dimensional model of CEM electron multiplication was established, and pulse FWHM and gain were calculated using the finite integration technique and a Monte Carlo method. The model is shown in Figure 11. Except for the protrusions, the geometric parameters followed Table 4. Because the numerous small wall protrusions were difficult to model individually, they were represented by an annular feature at the transition between the inlet cone and straight section. The equivalent feature had an outer diameter d, wall thickness T_P and height H_P, as shown in the enlarged view in Figure 11.

Two model conditions were evaluated (Table 6). Model 1 contained no protrusion and was used to compare the calculated pulse FWHM with the measured value for Case 2. Model 2 varied T_P to assess the effect of protrusion thickness on gain.

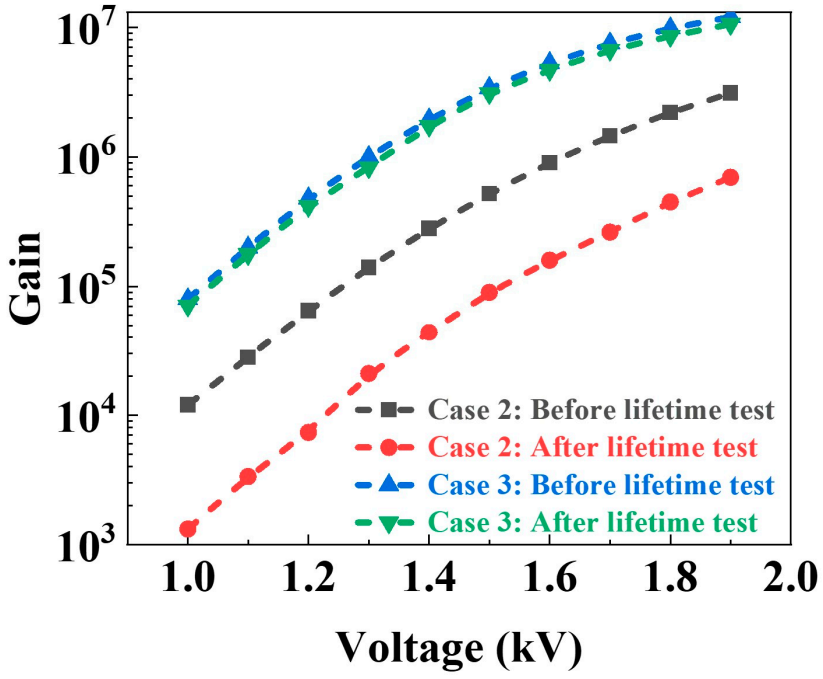


Figure 10. Analog gain before and after the accelerated lifetime test.

Table 6. CEM simulation conditions.

Model	Parameters
Model 1	$H_P = 0$; $T_P = 0$
Model 2	$H_P = 0.1$ mm; $T_P = 0$–0.4 mm, in 0.1 mm steps

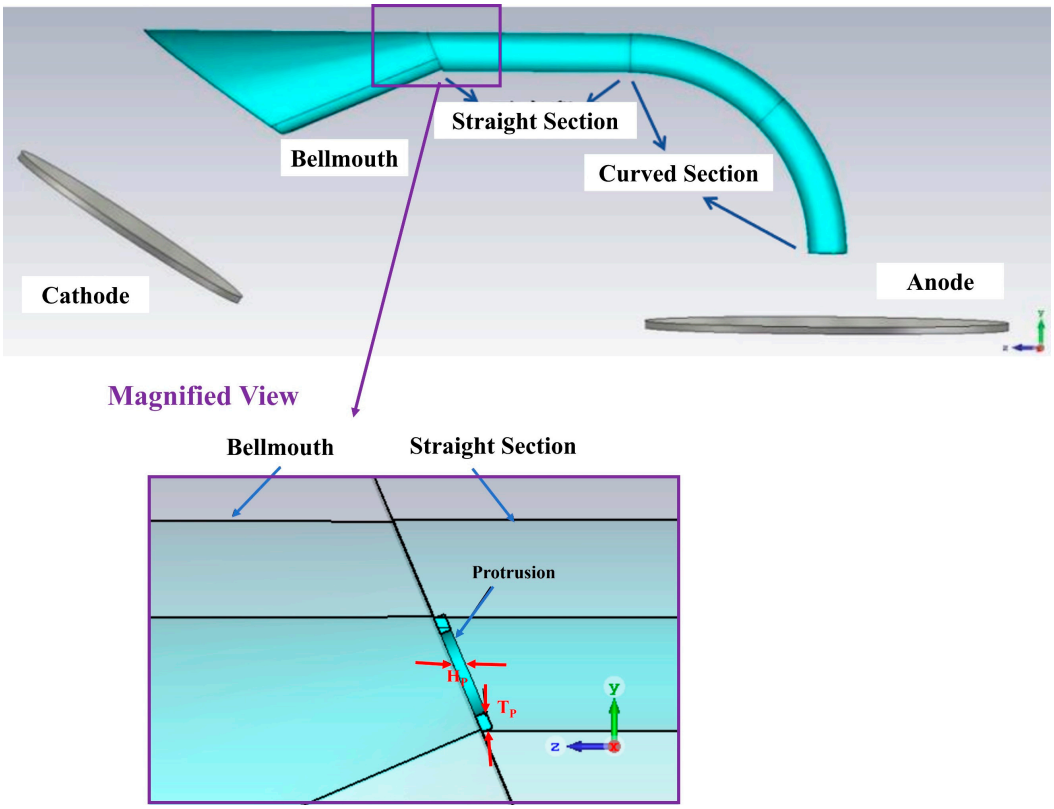


Figure 11. Three-dimensional CEM simulation model.

Figure 12 compares the simulated and measured pulse waveforms. Their overall trends were similar. The simulated FWHM was 6.4 ns and the measured FWHM was 8 ns. The simulated pulse was narrower and lacked the distortion observed during the falling edge of the measured signal, plausibly because the model omitted parasitic impedance, secondary emission at the anode and the response of the readout chain.

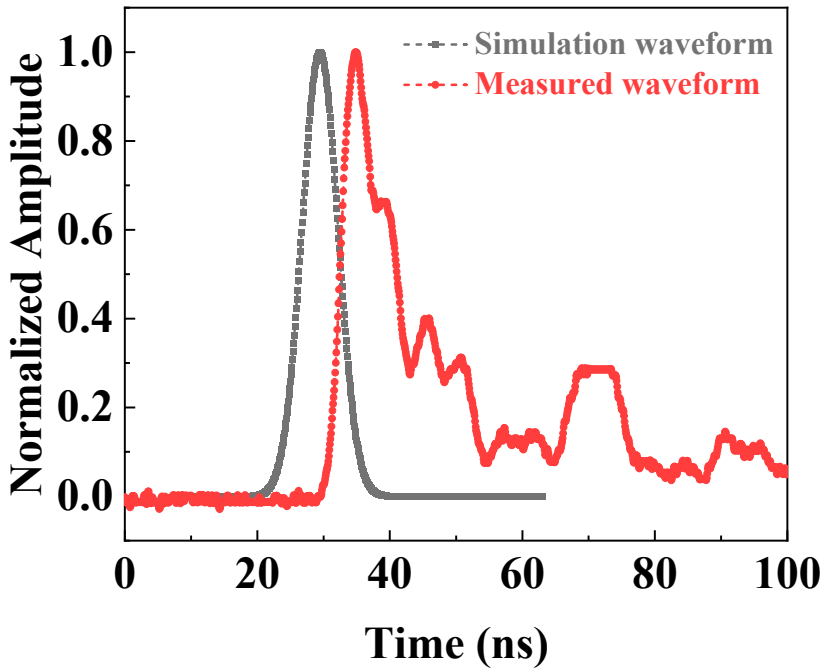


Figure 12. Simulated and measured pulse waveforms.

Figure 13 shows simulated gain and the number of secondary electrons available for further multiplication as a function of protrusion thickness at 2.0 kV. Gain initially increased and then decreased as thickness increased. The number of electrons available for further multiplication followed the same trend, indicating that a reduction in this population contributed to the gain decrease. Increasing protrusion thickness from 0 to 0.4 mm reduced pulse gain from 8.71×10^6 to 2.60×10^6, consistent with the trend in the gain measurements shown in Figure 8.

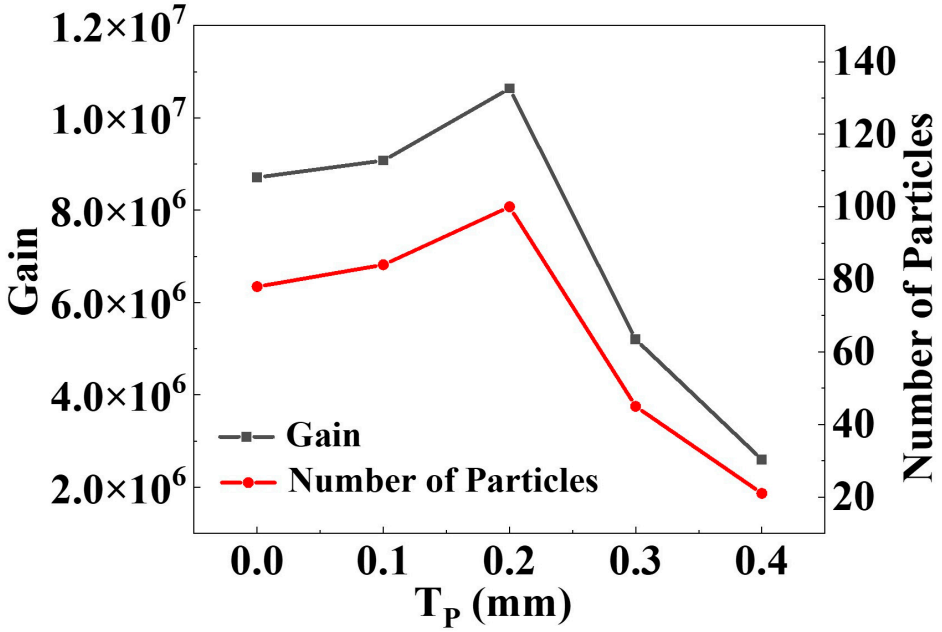


Figure 13. Simulated gain and number of electrons available for further multiplication versus protrusion thickness at 2.0 kV.

3.7. Surface-Science Interpretation

From a surface-science perspective, elemental Pb formed during hydrogen reduction can be dissolved by HCl, as represented by Equation (8); this is proposed to be the principal reason for the removal of the Pb particles in Figure 5. The CEM material contains 64.2% SiO_2, which can dissolve in NaOH solution through the overall reaction shown in Equation (9). Dissolution of elemental Pb by HCl and SiO_2 by NaOH is considered to have jointly contributed to the decrease in Rq from 1.28 to 0.15 nm shown in Figure 6. This interpretation is based on proposed overall reactions during alternating acid and base etching; the specific reactions occurring during the process require further study. The improved CEM lifetime after ALD may be attributable to the dense ALD film suppressing alkali-metal loss [15] and slowing gain degradation. The detailed suppression and operating mechanisms require further study.

$$Pb + 2HCl = PbCl_2 + H_2 \uparrow \quad (8)$$

$$SiO_2 + 2NaOH \rightarrow Na_2SiO_3 + H_2O \quad (9)$$

4. Conclusions

The CEM was fabricated from lead silicate glass by preform preparation, capillary drawing, inlet flaring, outlet bending, inlet shaping, cleaning, hydrogen reduction, sandblasting isolation, etching, electron-beam evaporation and atomic layer deposition. This study investigated the effects of alternating acid and base etching and ALD on channel electron multiplier performance. Alternating acid and alkaline etching reduced the root-mean-square roughness (Rq) from 1.28 to 0.15 nm. At 2.0 kV, pulse gain increased from 2.00×10^6 to 8.25×10^6, and dark count rate decreased from 54.23 to below 2 counts/s. A subsequently deposited Al_2O_3 film with a nominal thickness of 5.5 nm further increased pulse gain to 3.30×10^7. After an accumulated output charge of 0.158 C, analog gain loss at 1.0 kV decreased from 89% to 11%. The CST results followed the same trend as the measurements, indicating that wall protrusions can suppress secondary-electron multiplication. Alternating acid and base etching combined with ALD therefore substantially improved CEM gain, noise performance and lifetime. From a surface science perspective, we hypothesize that the hydrochloric acid solution dissolves elemental lead, whereas the sodium hydroxide solution dissolves silica. Their alternating action may contribute to reducing the roughness of the channel wall.

Author Contributions: Conceptualization, Z.H., X.C. and Y.Q.; methodology, Z.H., X.C. and Y.Q.; software, Z.H. and J.W.; validation, Z.H., H.Z. and Y.C.; formal analysis, Z.H.; investigation, Z.H., J.Z., H.Z., Y.C., P.N. and L.L.; resources, X.C., Y.Q. and S.L.; data curation, Z.H. and L.L.; writing—original draft preparation, Z.H.; writing—review and editing, X.C., Y.Q. and S.L.; visualization, Z.H. and P.N.; supervision, X.C. and Y.Q.; project administration, X.C.; funding acquisition, L.L. All authors have read and agreed to the published version of the manuscript.

Funding: This research was funded by the National Natural Science Foundation of China, grant numbers 12573105 and U2541225.

Institutional Review Board Statement: Not applicable.

Informed Consent Statement: Not applicable.

Data Availability Statement: The raw data supporting the conclusions of this article will be made available by the authors on request.

Acknowledgments: The authors thank the 718th Research Institute of China State Shipbuilding Corporation Limited (CSSC), the residual gas analyzer manufacturer, for its help in determining the cumulative CEM output charge over the device lifetime. During the preparation of this manuscript, the authors used ChatGPT-5.6(OpenAI) solely for formatting the manuscript. The author used ChatGPT-5.6 to assist in generating Figure 2. The authors have reviewed and edited the output and take full responsibility for the content of this publication.

Conflicts of Interest: The authors Zexun Hu, Xiaoqing Cong, Jiaqi Zhu, Heng Zhao, Jian Wang, Yan Cheng, Pengjie Niu, and Longhui Li were employed by North Night Vision Technology (Nanjing) Research Institute Co., Ltd., and Nanjing Branch of North Night Vision Technology Co., Ltd. The remaining authors declare that the research was conducted in the absence of any commercial or financial relationships that could be construed as potential conflicts of interest. The authors declare that this study received determining the cumulative CEM output charge over the device lifetime as support from 718th Research Institute of China State Shipbuilding Corporation Limited (CSSC). The company was not involved in the study design, collection, analysis, interpretation of data, the writing of this article or the decision to submit it for publication.

References

1. Adams, J.; Manley, B.W. The mechanism of channel electron multiplication. *IEEE Trans. Nucl. Sci.* **1966**, *13*, 88–99. https://doi.org/10.1109/TNS.1966.4324084.
2. Seah, M.P. Channel electron multipliers: Quantitative intensity measurement—Efficiency, gain, linearity and bias effects. *J. Electron Spectrosc. Relat. Phenom.* **1990**, *50*, 137–157. https://doi.org/10.1016/0368-2048(90)80015-3.
3. Reagan, N.R.; Frees, L.C.; Gray, J.W. Mass-dependent effects of channel electron multipliers in residual gas analyzers. *J. Vac. Sci. Technol. A* **1987**, *5*, 2389–2392. https://doi.org/10.1116/1.574460.
4. Malyshev, O.B.; Middleman, K.J. In situ ultrahigh vacuum residual gas analyzer "calibration". *J. Vac. Sci. Technol. A* **2008**, *26*, 1474–1479. https://doi.org/10.1116/1.2990856.
5. Mialle, S.; Quémet, A.; Ponvienne, A.; Gourgiotis, A.; Aubert, M.; Isnard, H.; Chartier, F. The use of total evaporation method using Channeltron electron multipliers by thermal ionization mass spectrometry for europium isotope ratio measurements on picogram sample amounts. *Int. J. Mass Spectrom.* **2012**, *309*, 141–147. https://doi.org/10.1016/j.ijms.2011.09.014.
6. Seah, M.P.; Gilmore, I.S.; Spencer, S.J. Signal linearity in XPS counting systems. *J. Electron Spectrosc. Relat. Phenom.* **1999**, *104*, 73–89. https://doi.org/10.1016/S0368-2048(98)00317-X.
7. Chen, L.; Zahng, B.; Liu, S.; Yan, B.; Peng, H.; Zhang, Y.; Luo, T. Optimization study on the collection efficiency of the channel electron multiplier in a UV photoelectron spectroscopy analyzer. *Opt. Contin.* **2025**, *4*, 1030–1039. https://doi.org/10.1364/OPTCON.550311.
8. Manalio, A.A.; Burin, K.; Rothberg, G.M. More efficient channel electron multiplier by coating of the cone with a high secondary electron yield material. *Rev. Sci. Instrum.* **1981**, *52*, 1490–1492. https://doi.org/10.1063/1.1136481.
9. Grzeszczak, A.; Kaszczyszyn, S.; Klein, S. Flicker noise of the channel electron multiplier. *Vacuum* **2000**, *57*, 99–104. https://doi.org/10.1016/S0042-207X(00)00113-5.
10. Grzeszczak, A.; Kaszczyszyn, S.; Klein, S. The spectral density of the electron multiplier noise in the analogue and the pulse counting mode. *Meas. Sci. Technol.* **2001**, *12*, L1–L3. https://doi.org/10.1088/0957-0233/12/2/101.
11. Grzeszczak, A.; Kaszczyszyn, S.; Klein, S. Dependence of the channel electron multiplier noise spectral functions on the parameters of its operation. *Vacuum* **2004**, *76*, 523–526. https://doi.org/10.1016/j.vacuum.2004.07.007.
12. Li, T.; Cong, X.; Wang, J.; Pan, K.; Li, W.; Jin, G.; Qiu, X.; Lin, Y. Mechanistic study on the micro-optical morphology and electrical properties of microchannel plates by acid–base alternating corrosion processes. *Silicon* **2024**, *16*, 719–727. https://doi.org/10.1007/s12633-023-02702-1.
13. Conneely, T.M.; Milnes, J.S.; Howorth, J. Extended lifetime MCP-PMTs: Characterisation and lifetime measurements of ALD coated microchannel plates, in a sealed photomultiplier tube. *Nucl. Instrum. Methods Phys. Res. A* **2013**, *732*, 388–391. https://doi.org/10.1016/j.nima.2013.07.023.

14. Cao, W.; Zhu, B.; Bai, X.; Xu, P.; Wang, B.; Qin, J.; Gou, Y.; Lei, F.; Liu, B.; Guo, J.; et al. High-sensitivity and long-life microchannel plate processed by atomic layer deposition. *Nanoscale Res. Lett.* **2019**, *14*, 153. https://doi.org/10.1186/s11671-019-2983-1.
15. Leitzenberger, M. Migration of Mobile Ions in Dielectric Semiconductor Compounds. Ph.D. Thesis, TU Wien, Vienna, Austria, 2023.

Disclaimer/Publisher's Note: The statements, opinions and data contained in all publications are solely those of the individual author(s) and contributor(s) and not of MDPI and/or the editor(s). MDPI and/or the editor(s) disclaim responsibility for any injury to people or property resulting from any ideas, methods, instructions or products referred to in the content.